Research Square

Preprints are preliminary reports that have not undergone peer review.
They should not be considered conclusive, used to inform clinical practice,
or referenced by the media as validated information.

Second-harmonic generation and the conservation of spatiotemporal orbital angular momentum of light

Guan Gui
JILA, University of Colorado Boulder
Nathan Brooks
JILA, University of Colorado Boulder
Henry Kapteyn
Joint Institute for Laboratory Astrophysics
Margaret Murnane
JILA, University of Colorado Boulder
Chen-Ting Liao (chenting.liao@gmail.com)
University of Colorado Boulder https://orcid.org/0000-0002-3423-277X

Article

Keywords: Space-time Spiral Phase Structure, Nonlinear Scaling Rule, Spatiotemporal Astigmatism, Multiple Phase Singularities, Nonlinear Conversion

Posted Date: December 10th, 2020

DOI: https://doi.org/10.21203/rs.3.rs-116263/v1

License: This work is licensed under a Creative Commons Attribution 4.0 International License.
Read Full License

Version of Record: A version of this preprint was published at Nature Photonics on July 5th, 2021. See the published version at https://doi.org/10.1038/s41566-021-00841-8.

SECOND-HARMONIC GENERATION AND THE CONSERVATION OF SPATIOTEMPORAL ORBITAL ANGULAR MOMENTUM OF LIGHT

GUAN GUI,[1] NATHAN J. BROOKS,[1] HENRY KAPTEYN,[1,2] MARGARET MURNANE,[1] AND CHEN-TING LIAO[1*]

[1]*JILA, University of Colorado and NIST, 440 UCB, Boulder, Colorado 80309, USA*

[2]*KMLabs Inc., 4775 Walnut Street, Suite 102, Boulder, Colorado 80301, USA*

[*]*chenting.liao@colorado.edu*

Abstract

Light with spatiotemporal orbital angular momentum (ST-OAM) is a recently discovered type of structured electromagnetic field with characteristic space-time spiral phase structure and transverse OAM. In this work, we present the first generation and characterization of the second-harmonic of ST-OAM pulses. By uncovering the conservation of transverse OAM in a second-harmonic generation process, where the space-time topological charge of the fundamental field is doubled along with the optical frequency, we establish a general nonlinear scaling rule—analogous to that describing the spatial topological charges associated with the conventional longitudinal OAM of light. Furthermore, we observe that the topology of a second-harmonic ST-OAM pulse can be modified by complex spatiotemporal astigmatism, giving rise to multiple phase singularities separated in space and time. Our finding thus confirms that a spatiotemporal phase winding, surrounding one or many phase singularities in space and time, can be interpreted as a new class of topological charge. Our study opens a new route for nonlinear conversion and scaling of light carrying ST-OAM with the potential for driving other secondary ST-OAM sources of electromagnetic fields, electron pulses, and beyond.

Introduction

The orbital angular momentum (OAM) of light is a type of angular momentum associated with phase front vortices in the electromagnetic field[1,2]. For a propagating paraxial wave, the longitudinal OAM of light means that the OAM is parallel to the averaged wavevector and propagation direction of the beam. In addition, OAM can be intrinsic or extrinsic –-intrinsic OAM implies that the angular momentum is independent of the choice of the reference frame and can be described by an integer quantum number called the (spatial) topological charge ℓ_c. The intrinsic longitudinal OAM (here referred to as conventional OAM) of light has an OAM of $\hbar\ell_c$ per photon and a spiral phase structure $e^{i\ell_c\Phi_c(x,y)}$, surrounding a phase singularity in the x-y plane (see Fig. 1a). Most research efforts over the past three decades have focused on conventional OAM of light, which has impacted many important applications — including optical tweezers, super resolution imaging, quantum and classical communication, and others[3–5 ,9]. Very recently, pulses with time-varying OAM, or self-torque, have been discovered[18].

In contrast, a transverse OAM of light implies that the OAM is perpendicular to the averaged wavevector of the beam. This means that a spiral phase structure resides in space-time, e.g., the x-t (or equivalently, the x-z) plane in a simplified 2D case (see Fig. 1a), and is thus referred to as spatiotemporal orbital angular momentum (ST-OAM). By analogy with conventional OAM, we can designate an integer ℓ as the spatiotemporal topological charge to describe the space-time winding phase $e^{i\ell\Phi(x,z,t)}$. The scalar field of an ST-OAM pulse reads -

$$E\ (x,y,z,t) \propto E_0(x,y,z)e^{i\ell\Phi(x,z,t)}e^{i(k_z z-\omega t)}, \qquad [1]$$

where E_0 is the field envelope including the assumed Gaussian profile in the y-axis for simplicity. This transverse OAM of light was theoretically predicted[8,9], and generated through a nonlinear self-focusing process[10]. Very recently, optical pulses with ST-OAM were experimentally realized

in the linear regime for the first time[11,12]. We note that the ST-OAM of light was only recently discovered, and many of its properties are still not known. Therefore, the extent to which they can be described by an analogy with the conventional OAM of light remains unclear.

In nonlinear frequency conversion, the conventional OAM of light follows a simple scaling rule, where the N-th harmonic has a topological charge $N\ell_c$, reflecting OAM conservation. This rule has been verified for SHG [13,14], non-perturbative high-order (N >10) harmonic generation[15], and can be generalized to describe sum- or difference-frequency generation processes[16]. Note that this rule only applies to scalar fields without spin angular momentum, otherwise total angular momentum conservation must be included[17].

In this manuscript, we experimentally investigate the behavior of ST-OAM pulses during the frequency up-conversion process of second-harmonic generation (SHG). By experimentally uncovering the conservation of ST-OAM in a second-harmonic generation process, where the space-time topological charge of the fundamental field is doubled along with the optical frequency, we establish a general nonlinear scaling rule for the first time—analogous to that describing the spatial topological charges in conventional OAM of light. We also investigate the effects of spatiotemporal astigmatism in SHG, which leads to non-conserved topological changes of the spiral phase structure, and the creation of multiple phase singularities separated in space-time. Our finding thus confirms that this spatiotemporal phase winding, surrounding one or many phase singularities in space and time, can be interpreted as a new class of topological charge.

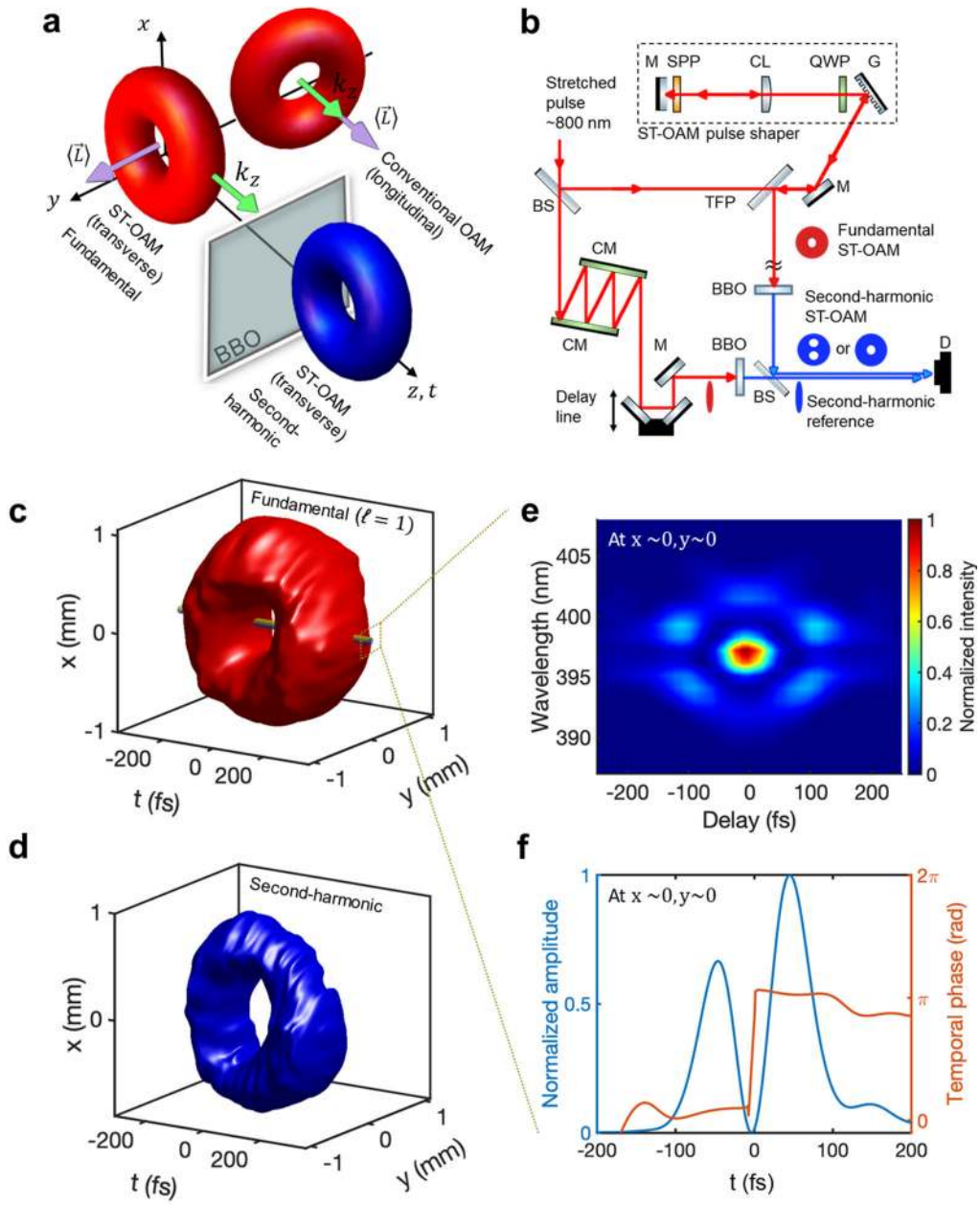

Fig.1 | Second-harmonic spatiotemporal orbital angular momentum (ST-OAM) pulse generation and characterization. a. Schematic of longitudinal (conventional) OAM of light, transverse ST-OAM of light, and its second-harmonic generation (SHG). All pulses are represented by their isosurface intensity profiles. The averaged OAM $\langle\vec{L}\rangle$ (purple arrows) in a conventional OAM pulse is parallel to or aligned with the propagation direction k_z (green arrows), and thus named longitudinal OAM, while the averaged OAM in an ST-OAM pulse is perpendicular to the propagation direction and thus named transverse OAM. **b.** In the experiment, fundamental ST-OAM pulses of topological charge ℓ=1 are generated by a custom pulse shaper. The pulses carry an azimuthal spatiotemporal phase swirl structure in the x-z plane, parallel to the beam propagation direction along the z-axis. Second-harmonic ST-OAM pulses are generated in a BBO crystal and then characterized by interference with a reference Gaussian pulse. **c.** Experimentally reconstructed 3D intensity isosurface profile of the fundamental ST-OAM pulse and its second-harmonic shown in **d.** The intensity profile shows a singularity structure in space and time at the center. The center part of the fundamental ST-OAM pulse (indicated by the brown bar) was experimentally sampled and characterized by a FROG setup, where the measured FROG trace and the reconstructed temporal electric field envelope and the temporal phase are shown in **e** and **f**, respectively. M: mirror; DM: dichroic mirror; CM: chirped mirror; CL: cylindrical lens; BS: beam splitter; TFP: thin film polarizer; QWP: quarter wave plate; SPP: spiral phase plate; G: grating; BBO: beta barium borate crystal; D: detectors including a beam profiler and a FROG setup.

Results

The generation and measurement of light with ST-OAM and its second-harmonic. The generation of ST-OAM pulsed beams is depicted in Fig. 1b. A fundamental pulse at central wavelength $\lambda = 800$ nm from a Ti:Sapphire amplifier is sent to a custom ST-OAM pulse shaper to generate light with ST-OAM of $\ell = 1$ (see **Methods**). Unlike conventional OAM beams which can be characterized by space-based methods such as fork hologram[19], coherent diffractive imaging[20], structured apertures[21], ST-OAM pulses require a space-time or equivalently space-frequency based characterization method. Figures 1c and 1d show experimentally measured and reconstructed 3D intensity isosurface profiles of the fundamental and second-harmonic ST-OAM pulse, respectively.

Interestingly, we realized that a common frequency-resolved optical gating (FROG) setup can also be used to measure the spatiotemporal phase structure of an ST-OAM pulse by carefully placing an entrance pinhole at different positions of the beam and scanning over it. Figures 1e and 1f show a typical FROG trace and its reconstruction from a fundamental ST-OAM pulse of $\ell = 1$, measured at the beam center. In Fig. 1f, the field amplitude envelope reconstruction clearly shows a double-pulse structure in the time domain, and the retrieved temporal phase shows a clear π phase jump between the front and rear ends, consistent with the expected 2π phase shift along the azimuth in the x-t plane and a centered phase singularity. Although doable, a spatially resolved FROG measurement is tedious with slow throughput and known to have ambiguities on nontrivial time direction, absolute phase, and temporal shift. Therefore, we used a Mach-Zehnder-like scanning interferometer to optically gate an ST-OAM pulse to fully characterize an ST-OAM pulse and its second-harmonic.

Briefly, a long, 800-nm fundamental, ST-OAM pulse of ~500 fs of $\ell = 1$ was interfered with a short, 800-nm fundamental, Gaussian reference pulse of ~45 fs to form interference fringes. These fringes characterize the portion of the ST-OAM pulse gated by the >10x shorter reference pulse. By scanning the time delay, the spatiotemporal profile of the ST-OAM pulse can be reconstructed computationally from the delay-dependent fringes, where each delay is a time frame of the reconstruction (See **Methods)**. Some representative fringe patterns of ST-OAM pulses are shown in Fig. 2, with two black markers added to each time frame as a visual guide to the eye to observe the fringe shift. The discontinuous phase jump (or phase dislocation) around the singularity happens close to delay zero. When the reference pulse was scanned towards the ST-OAM phase singularity (-300 to 0 fs), the fringes are first tilted, and then shifted by a π phase difference at the center of the singularity. When the reference pulse was scanned away (0 to 300 fs), the fringes become straight again, but the upper and lower fringes were shifted by one fringe. Such a fringe shift is a feature of an ST-OAM pulse of $\ell = 1$. The reconstructed spatiotemporal amplitude and phase of the fundamental ST-OAM pulse are shown in Fig. 2a-c, based on the fringe data shown in Fig. 2d. Figure 2a is the amplitude envelope, 2b is the phase, and 2c is a complex field representation where the amplitude and phase are represented by brightness and hue, respectively. Our experimentally reconstructed spatiotemporal profiles clearly confirm the generation of a vortex-shaped ST-OAM pulse with a 2π azimuthal phase swirl in space and time.

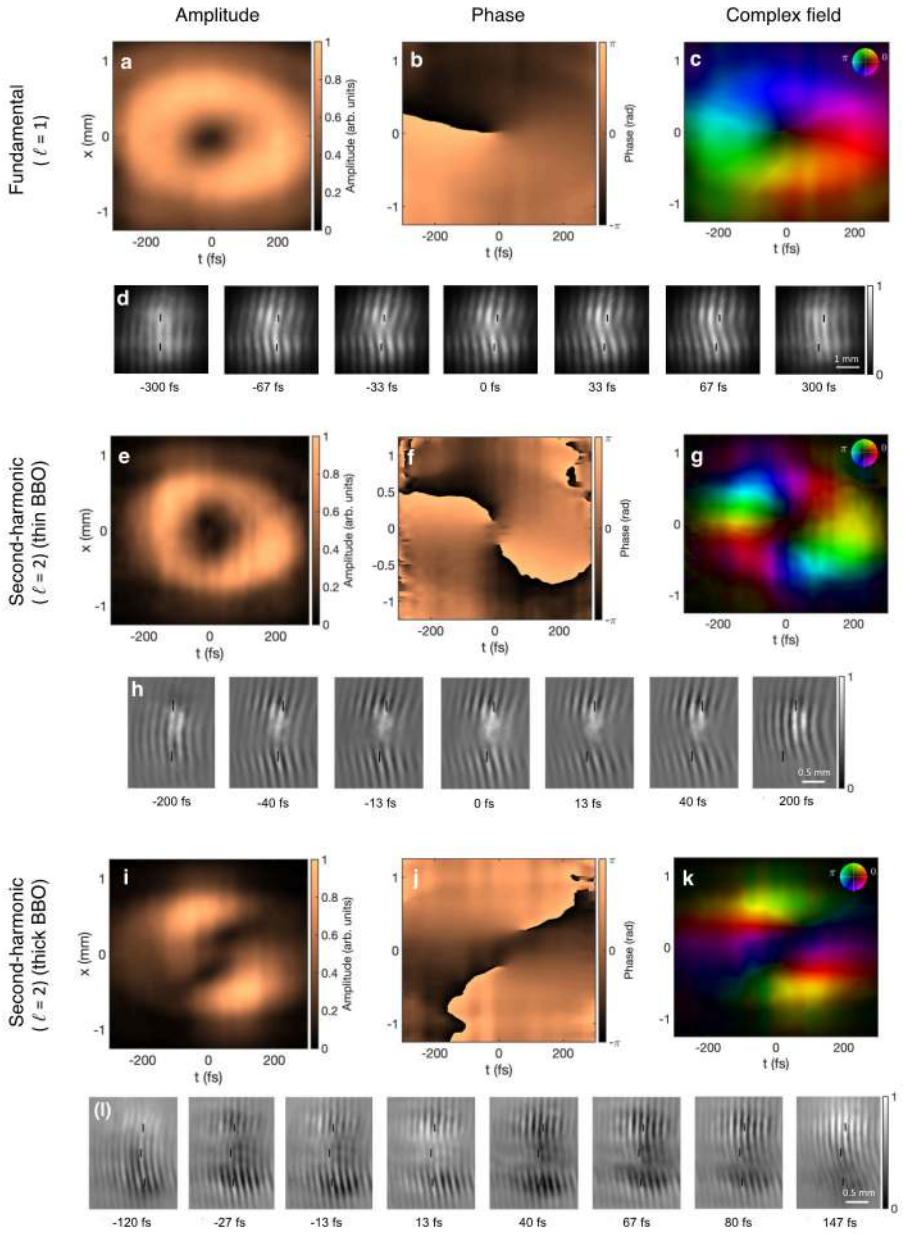

Fig.2 | Experimentally reconstructed amplitude and phase of ST-OAM pulses. A fundamental ST-OAM pulse of topological charge ℓ =1 was measured and reconstructed to show its **a,** amplitude envelope, **b,** phase, and **c**, complex field representation by a scanning interferometer. Representative fringe patterns at various time delays obtained from the interferometry are shown in **d,** with two black markers added as an aid to the eye to observe the fringe shift. The phase profile in a fundamental ST-OAM pulse shows the 2π spiral phase accumulation on traversing a closed spatiotemporal path around the singularity. A second-harmonic ST-OAM pulse generated by a thin BBO crystal was measured and reconstructed using the same method to show its **d,** amplitude envelope, **e,** phase, **f**, complex field representation, and **g.** representative fringe patterns. The results show that the spatiotemporal topological charge is also doubled after frequency doubling, evidenced by the 4π phase accumulation. The SHG with topological charge ℓ =2 indicates the conservation of ST-OAM. A second-harmonic ST-OAM pulse was also generated by a thick BBO crystal and measured in **h,** amplitude envelope, **i,** phase, **j**, complex field representation, and **k,** representative fringe patterns. The OAM is still conserved in this case, but the two singularities are generated and separated further in both space and time, comparing to the case in a thin BBO crystal. The color wheels for complex field representation are shown at the top right corners of **a, g, k**, where amplitude and phase are represented by brightness and hue, respectively.

Second-harmonic fields were generated by sending the fundamental pulses through individual BBO crystals on two arms of a similar interferometer. Therefore, we obtained a long, 400-nm second-harmonic, ST-OAM pulse of an unknown, to-be-determined charge ℓ, and a short, 400-nm second-harmonic, Gaussian reference pulse to form interference fringes. A second-harmonic ST-OAM pulse generated by a thin BBO crystal (20 μm in thickness) is experimentally reconstructed and shown in Fig. 2e, 2f, and 2g. Figure 2h shows the fringe patterns used for reconstruction, also with black markers added as visual aids, where we can see the upper and the lower parts of the pattern are shifted by two fringes, indicating a 4π phase shift when moving across the singularity. The amplitude envelope profile of the second-harmonic pulse still looks close to a simple vortex shape, which shares the same topology with the fundamental ST-OAM pulse: a torus of genus close to one. Although the reconstructed phase profile shows two singularities, they are almost overlapped in the time domain and slightly dislocated in space by only ~200 μm, approximating a single phase singularity with 4π azimuthal spiral phase in space-time. The small singularity separation can be attributed to a slight offset of the laser central wavelength to the design SPP wavelength, and/or a slight amount of astigmatism of the initial Gaussian beam. Also, the generation of the fundamental spatial OAM beams are far from perfect inside the pulse shaper—they are generated slightly off the Fourier plane of the 4-f pulse shaper because we relied on the beam double passing through the same SPP by retroreflection.

The 4π spiral phase we observed indicates that the second-harmonic ST-OAM pulse has a confirmed spatiotemporal topological charge of $\ell = 2$ after frequency doubling. Therefore, we established a nonlinear scaling rule and uncovered that the spatiotemporal angular momentum is conserved during an SHG process.

Spatiotemporal astigmatism and modal analysis. We also investigated a case with strong spatiotemporal astigmatism by generating second-harmonic ST-OAM pulses using a thick (1 mm) BBO crystal, as shown in Figs. 2i, j, and k. Unlike the thin BBO case, the second-harmonic pulse from a thick BBO crystal has a different topology in the pulse profile – there are two amplitude holes (two phase singularities) close to the center with two outer lobes — a case resembling a torus of genus two. The phase profile in Fig. 2j shows two phase singularities with a 2π spiral phase individually, giving rise to a 4π accumulated phase. This again demonstrates ST-OAM conservation in an SHG process, although the topology is not conserved. The two phase singularities are dislocated in both time, by ~50 fs, and in space, by ~500 μm.-We note that this separation is recently predicted and presented in a simulation[22]. Such separation of phase singularities in the x-t plane can also be observed directly from the fringe patterns in Fig. 2l, where the upper, middle, and lower parts of the pattern are shifted at various time and spatial locations. The use of a thicker BBO crystal leads to spatiotemporal astigmatism including phase mismatch and group velocity mismatch. The phase mismatch narrows the frequency conversion bandwidth and the group velocity mismatch stretches the second-harmonic pulse duration. Consequently, the second-harmonic ST-OAM pulses are distorted in space and time, causing a change in topology of the vortices.

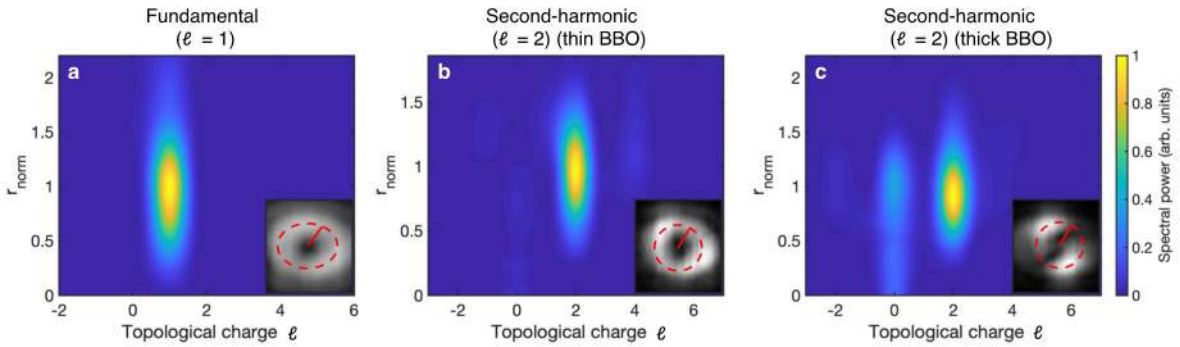

Fig. 3 | Modal decomposition of the ST-OAM pulses. OAM mode spectra of the ST-OAM pulses from **a**, fundamental pulses, **b**, second-harmonic pulses generated by a thin BBO, and **c**, second-harmonic pulses generated by a thick BBO. The modal decompositions are obtained by Fourier transformation of the measured spatiotemporal phase along the azimuthal direction on the x-t plane for different normalized polar radii r_{norm}. The radii are shown in solid red lines in the insets overlapped with their corresponding amplitude envelope profiles for reference. The color map corresponds to the power spectrum in arbitrary units. In **a**, the ℓ = 1 charge contains ~94.5% of the total spectral power. In **b** and **c**, the ℓ = 2 charge contains ~80.9% and ~57.8% of the total power, respectively.

To quantify how these ST-OAM pulses are distorted by imperfect SHG conditions, we performed a modal decomposition of the ST-OAM pulses. The OAM mode spectra are calculated by Fourier transformation over the reconstructed phase profiles along the azimuthal direction on the x-t plane for normalized polar coordinates r_{norm}. Unlike a conventional OAM beam where the x- and y-axes are equivalent, ST-OAM pulses need to be scaled in the x-axis and the t- (z-) axes to obtain the mode spectrum correctly (See **Methods)**. The insets in Fig. 3 show how the origins in the polar coordinates and scaling factors are defined in each case to deal with a different number of phase singularities, where the solid red lines are overlapped with amplitude envelope profiles taken from Figs. 2a, e, and i for reference. The mode spectra are shown in Fig. 3a for the fundamental pulses, 3b for the second-harmonic pulses generated using a thin BBO crystal, and 3c for the second-harmonic pulses generated using a thick BBO crystal. As expected, the peak of the ST-OAM spectrum is located at ℓ = 1 for the fundamental ST-OAM pulse and mainly at ℓ = 2 for its second-harmonic field.

To calculate how much spectral power is located at the expected charge number, each mode spectrum was integrated along the radial coordinate. For the fundamental pulse, ~94.5% of the

total spectral power is located at ℓ = 1 (Fig. 3a). For the second-harmonic pulses generated using a thin BBO crystal in Fig. 3b, the majority (~80.9%) of the total power is at ℓ = 2 (Fig. 3b), reflecting the conservation of ST-OAM in the SHG process. However, in the case of a thick BBO crystal, we observed severe degradation or increased impurity of the modal spectrum, where only ~57.8% of the total power is at ℓ = 2 and a significant DC peak appears (Fig. 3c). This result indicates that the second-harmonic ST-OAM field is distorted after the generation and propagation through the thicker crystal due to spatiotemporal astigmatism.

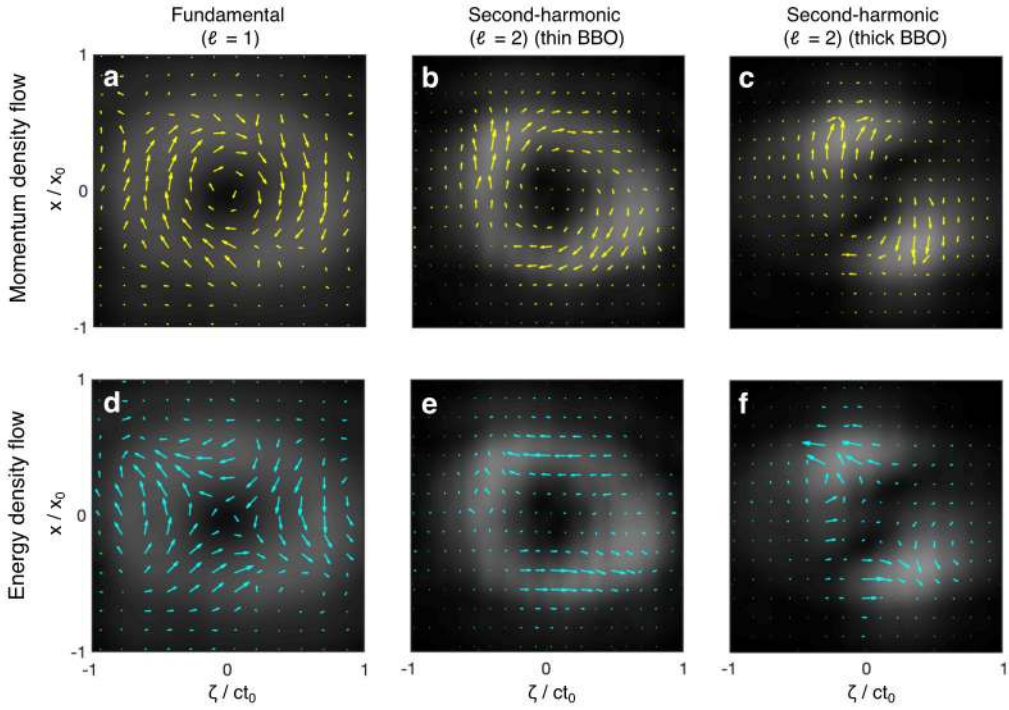

Fig.4 | Spatiotemporal momentum and energy density flows of ST-OAM pulses. A momentum density flow, which is proportional to the imaginary part of the scalar field complex conjugate multiplying the field gradient, is calculated in **a,** a fundamental ST-OAM pulse, **b,** its second-harmonic ST-OAM pulse generated by a thin BBO crystal, and **c,** its second-harmonic ST-OAM pulse generated by a thick BBO crystal. The ratio of ST-OAM per pulse $\ell^{2\omega}/\ell^{\omega}$ is 2.09, comparing b. to a., and 1.36, comparing c. to a. An energy density flow in the BBO crystal, which is proportional to the phase gradient and the dispersion, is calculated in **d,** a fundamental ST-OAM pulse, **e,** its second-harmonic ST-OAM pulse generated by a thin BBO crystal, and **f,** its second-harmonic ST-OAM pulse generated by a thick BBO crystal. The amplitude of the momentum density flow vectors (the length of the yellow arrows) are scaled by $1/ct_o$ along the ζ-axes and by $1/x_0$ along the x-axis for better visualization. On the contrary, the amplitude of the energy density flow vectors (the length of the cyan arrows) is not scaled to show the original orientation of energy flow directly. The grayscale backgrounds are amplitude envelope profiles taken from Fig. 2a, 2e, 2i for reference. ST OAM pulses propagate from the left to the right of the figures.

The momentum and energy density flow of second-harmonic ST-OAM of light. We next investigated the momentum and energy density flow of the fundamental and its second-harmonic ST-OAM pulses to better understand the SHG process including spatiotemporal astigmatism. Given a scalar field $E = E_0 e^{i\psi}$, the momentum density flow is defined by $\vec{P} = \mathrm{Im}(E^* \nabla E)$.[23] Such momentum density flow can be further used to calculate a single quantity, ST-OAM per pulse ℓ (see **Methods**). Adopting this definition, Figs. 4a-4c show our experimentally measured "spatiotemporal" momentum density flows for a fundamental pulse in 4a, and its second-harmonic pulse generated using a thin and a thick BBO crystal in 4c and 4b. respectively. The amplitude of the momentum density flows ($|\vec{P}|$, the length of the yellow arrows) are scaled by $1/ct_o$ and by $1/x_0$ in the horizontal and vertical axes for a better visualization.

The momentum density flows of a fundamental ST-OAM pulse follow the gradient of the phase and form a vortex around the singularity. For a second-harmonic ST-OAM pulse in a thin BBO crystal, the momentum density flows are no longer uniformly distributed, but they still form a vortex. In this case, we obtain the ratio of ST-OAM per pulse $\ell^{2\omega}/\ell^{\omega} = 2.09$, the scenario of a perfect SHG process. However, for case in a thick BBO, the momentum density flows are redistributed following the distorted amplitude profile, resulting in the reduced ratio $\ell^{2\omega}/\ell^{\omega} = 1.36$. The smaller ST-OAM per pulse ratio is consistent with the appearance of a significant DC peak in the modal spectrum in Fig. 3c, similarly reflecting the degradation and the reduced mode purity due to spatiotemporal astigmatism in a thick crystal.

To further understand the physical mechanism responsible for this astigmatism, we calculated the energy density flow in our ST-OAM pulses. The spatiotemporal energy density flow can be written as $\vec{j} = \mathrm{E}^2[\nabla\psi - \mathrm{GVD}(\partial\psi/\partial\zeta)\hat{\zeta}]/\mathrm{k}$, following references[8,10], where GVD is the dimensionless group velocity dispersion of the material. In Fig. 4d-4f, the amplitude of the energy

density flows ($|\overrightarrow{J}|$, the length of the cyan arrows) are presented without rescaling, so we can observe the energy flow directly. In a fundamental ST-OAM pulse, the energy flows form a saddle-shaped antivortex structure around the singularity, given the positive GVD at this wavelength for BBO. As a fundamental ST-OAM pulse propagates through a thin BBO crystal, the SHG process, as well as a small amount of dispersion, leads to minor energy redistribution. In the case of a thick BBO crystal, larger dispersion can significantly reshape the ST-OAM pulses, leading to strong spatiotemporal astigmatism in the second-harmonic ST-OAM pulse. In Fig. 4d-4f, our calculated energy density flows in the BBO crystal show a tendency to reshape the ST-OAM pulse into a two-lobe structure upon continued propagation, resulting in the higher degree of distortion observed for the pulse emerging from the thick BBO crystal.

Discussion

The conservation of ST-OAM and space-time topological charges. The second harmonic ST-OAM pulse generated using a thin BBO can be described by a simple theory. In a simple scenario with perfect phase matching and an undepleted pump approximation, assuming a lossless medium, the second-harmonic field is proportional to the square of the complex input fundamental field, namely,

$$E^{(2\omega)}(x,y,\zeta) = E_0 e^{i\ell^{(2\omega)}\Phi(x,y,\zeta)} \propto [E^{(\omega)}(x,y,\zeta)]^2 \propto [e^{i\ell^{(\omega)}}]^2 \propto e^{i2\ell^{(\omega)}}, \qquad [2]$$

where $\zeta \equiv z - \mathrm{v}_g t$ is the space coordinate in the moving reference frame of a pulse traveling with the group velocity v_g. The definition of the field follows Eq. 1. As a result, $e^{\ell^{(2\omega)}} = e^{2\ell^{(\omega)}}$ and we obtain $\ell^{(2\omega)} = 2\ell^{(\omega)}$, indicating that space-time topological charge doubling when the optical frequency is doubled. In this scenario, the field profile of the second-harmonic wave should mimic the fundamental pulse. Because the pulse duration and the beam size of a fundamental pulse can

be shortened and reduced in a perfect SHG process due to its quadratic response, it partially explains the fact that the second-harmonic ST-OAM pulse shown is thinner as shown in Figs. 1c and d, and Figs. 2e and c.

It is worth mentioning that in the recent study[12], the authors argue that the spatiotemporal topological charge ℓ, which is associated with the total OAM, includes both *intrinsic* OAM and *extrinsic* OAM. Specifically, the intrinsic part still has OAM in the expression of $\hbar\ell_c$ per photon, as the conventional OAM of light. The other part expressed as $k_z\hbar x$, is the extrinsic OAM, which depends on the reference frame but not the charge ℓ_c. That is,

$$\hbar\ell \ = intrinsic \text{ OAM} + extrinsic \text{ OAM} = \hbar\ell_c + k_z\hbar x \qquad [3]$$

Thus, this expression implies that the ST-OAM of light carries the same amount of intrinsic OAM as the conventional OAM of light, but with an added, reference-frame dependent term. As a result, we argue that this viewpoint implicitly suggests and agrees with the conservation of ST-OAM in an SHG process we observed: in a second-harmonic or N-th harmonic generation process, we thus get $N\hbar\ell = N\hbar\ell_c + k_z\hbar x$, because the integration of the second term around the phase singularity and the y-axis vanishes for either fundamental or the harmonic field, regardless of its dependence (or independence) of the nonlinear conversion. Consequently, this result provides the other perspective in the SHG and the conservation of ST-OAM of light and agrees with our simple SHG theory in Eq. 2, given an ideal, phase-matched case.

The nonlinear relationship between the electric field amplitudes of a fundamental and its second-harmonic field means that the amplitude profile of the ST-OAM pulse changes during frequency doubling. Beyond the simple scenario, the SHG process is further complicated by additional factors in addition to phase mismatches, such as group velocity mismatch, intrapulse group velocity dispersion, absorption or losses, and pump depletion[24,25]. A rigorous theoretical

study of a final second-harmonic ST-OAM pulse profile must take the above factors into account and is the subject of further detailed investigation, which is beyond the scope of this manuscript.

Implications and applications of ST-OAM of light and its second-harmonic field. There could be many potential applications in ST-OAM pulses carrying transverse OAM. Conventional OAM beams carry spatial wavefront structures and are suitable for spatial domain applications such as enhanced imaging and novel scatterometry[5]. ST-OAM pulsed beams could enable new spatiotemporal applications using its temporal profiles for mechanical and thermal acoustic manipulation of particles, charges, phonon, or spins—space-time singular optics and its interactions with matter. For instance, even a simple photoemission or photoionization experiment using a conventional OAM beam provides a wealth of new phenomena[26], so we expect new effects and potentially new selection rules could be revealed by ST-OAM beams. It has also been demonstrated that the angular momentum carried by conventional OAM beams can be transferred to objects, leading to applications such as optical tweezers or spanners[27–29]. In analogy to this idea, it is theoretically possible to design a "spatiotemporal optical tweezer or spanner" with ST-OAM pulses for ultrafast manipulation of particles in both spatial and time domain, including new applications such as microtexturization of implant surfaces. Other applications based on the unique space-time momentum and energy density flows could be demonstrated in particle acceleration using structured spatiotemporal nonlinear wakefields[30]. Conventional OAM beams also provide a new degree of freedom in photons that can be utilized for multiplexing in telecommunication and quantum entanglement — therefore, we anticipate that the ST-OAM of light provides yet another degree of freedom that could unveil new routes in multiplexing—with a time domain perspective added such as phase and time-bin encoding[31].

Importantly, our demonstration of the ST-OAM nonlinear conversion and the ST-OAM conservation shows that a new avenue of secondary sources with ST-OAM can be realized experimentally in up-converted and likely down-converted electromagnetic waves. For example, it would be of interest to investigate the stimulated OAM Raman scattering,[32] harmonic spin-orbit angular momentum cascade,[33] or entangled photons generated by parametric processes with ST-OAM pulses. It is also possible that other matter waves such as electron vortex beams or electron bunches with ST-OAM can be generated through photoelectron generation or other means to improve accelerator technologies and electron microscopy[34].

Conclusion. In summary, we report the first experimental observation of a second-harmonic ST-OAM pulsed beam and its space-time topological charge conversation during frequency doubling. The charge of the ST-OAM pulse, corresponding to the space-time spiral phase structure, was observed to double in the SHG process. Our finding also confirms that the spatiotemporal phase singularities in an ST-OAM pulse can be interpreted as a new class of space-time topological charges carrying transverse OAM, the term coined in analogy to the spatial topological charges in a conventional OAM beam carrying longitudinal OAM—both types of OAM follow the same charge conservation and scaling rules. We also found that the topological structure of the space-time phase swirl in a second-harmonic field may not be conserved and an SHG process can generate additional phase singularities, depending on spatiotemporal astigmatism due to group velocity mismatch or phase mismatch condition. SHG is the foundation of any nonlinear optics textbook. Our work thus opens a new avenue of light carrying ST-OAM in nonlinear conversion and scaling, and it further suggests the possibilities to drive secondary ST-OAM sources from electromagnetic waves, thermoacoustic waves, to matter waves.

Methods

ST-OAM pulse generation. A stretched (full width at half maximum pulse duration ~ 500 fs) optical pulse at a central wavelength ~800 nm from a regenerative Ti:sapphire amplifier at 1 kHz repetition rate (KMLabs Wyvern HE) was first split into two paths before entering into a homemade Mach-Zehnder-type scanning interferometer. One path is for generating a short (~45 fs), Gaussian reference pulse, and the other is for generating a long (~500 fs) ST-OAM pulse. The reference Gaussian pulses were compressed using dispersive chirped mirrors (CM, Ultrafast Innovations) with multiple bounces to shorten the pulse duration. The ST-OAM pulses were generated by a custom pulse shaper we designed, consisting of a reflective grating (600 grooves/mm), a cylindrical lens (f = 25 cm), a multi-faceted spiral phase plate (SPP, HoloOr, 16-steps per phase wrap), and a high-reflectance end mirror for retroreflection. To generate fundamental ST-OAM pulses of spatiotemporal topological charge $\ell = 1$, an SPP with designed spatial topological charge $\ell_c = 0.5$ at the design wavelength 790 nm was used. Upon a retroreflection from the end mirror, the pulse passes through the SPP twice and generates the desired spatial topological charge $\ell_c = 0.5 - (-0.5) = 1$. Note that an SPP is a non-reciprocal optical component and a mirror reflection changes the sign of the ℓ_c, thus, the double-passing of the SPP from the opposite direction makes the ℓ_c charge addition possible, when the two passes are very close. A Fourier transform in the spectral domain of the pulse shaper converts a spatially chirped beam with a spatial spiral phase into a pulsed beam with a spatiotemporal spiral phase. Beta barium borate (BBO) crystals with thickness 20 μm (thin BBO) and 1 mm (thick BBO) cut and oriented to phase match type-I SHG are used to generate the second-harmonic at 400 nm, which are placed in the far field from the pulse shaper. The second-harmonic Gaussian reference pulse was generated by another 200-μm thick type-I SHG BBO crystal. To avoid any distortion and diffraction of the spatiotemporal phase structure after focusing the pulse, we used a nearly collimated ST-OAM beam in the SHG process, without additional optics that will cause astigmatism in space and time[35].

The amplitude and phase reconstruction-FROG. Fundamental ST-OAM pulses were first measured using an SHG frequency-resolved optical gating (FROG) setup (videoFROG, MesaPhotonics) with an added small aperture to spatially sample the center of the beam. The field amplitude $|E_0(x = 0, y = 0, t)|$ and the phase $\Phi(x = 0, y = 0, t)$ were then iteratively

reconstructed using the measured FROG trace. In the FROG measurements, we used a compressed ST-OAM pulse with a shorter pulse duration for easier implementation in the FROG setup, in comparison with the longer ST-OAM pulse shown in Fig. 1c. Note that given sufficient spatial samplings over the beam, a FROG setup can characterize the spatiotemporal field profile of an ST-OAM pulse, although the procedure is tedious and time consuming. Also, the SHG FROG used here is known to have ambiguities on nontrivial time direction, absolute phase, and temporal shift.

The amplitude and phase reconstruction-interferometer. Both fundamental and second-harmonic pulse amplitude $|E_0|$ and phase Φ were measured using a Mach-Zehnder-type scanning interferometer. When scanning the time delay between a short reference pulse and a long ST-OAM pulse, the reference pulse serves as an optical gating pulse that provides spatial information of both amplitude and phase at the given time delay. We used 38 delays to reconstruct fundamental ST-OAM pulses and >50 delays for second-harmonic ST-OAM pulses. To reconstruct the 3D amplitude profile $|E_0(x, y, t)|$, we first extracted the envelope of the fringe patterns at various time delays. At each time delay, the fringe envelope was then divided by the amplitude of the reference beam, which gives the 2D amplitude of the ST-OAM pulse at each delay. By stacking 2D amplitude profiles at various time delays, a 3D amplitude reconstruction is retrieved. We then used them to calculate and present 3D intensity isosurface profiles, with 37% energy of the wave contained in the torus-shaped isosurface, as shown in Fig. 1c & 1d. On the other hand, the 2D amplitude profiles shown in Fig. 2 are projections along the y-axis of the 3D amplitude profiles on to the x-t plane, $|E_0(x, t)|$. To reconstruct the phase, we first applied 1D Fourier transform to the original fringe patterns along the y-axis. By extracting the phase of the AC peak in the Fourier domain, we obtained a 1D phase profile from each 2D fringe pattern, representing $\Phi(x)$ at each time delay. The 2D phase reconstruction is retrieved by stacking 1D profiles at each time delay. It is worth mentioning that due to the instability of the interferometer, the position of the fringe patterns can vary shot-to-shot. To overcome this problem, the delay-dependent 1D phase profiles were numerically shifted by constant phases, which are calculated by the amplitude-weighted least square method to achieve the best phase continuity (smoothness) in the time domain. Besides, all phase profiles were subtracted by the same background to minimize linear phases and the trivial temporal phase $e^{-i\omega t}$ is omitted. Both amplitude and phase reconstructions in Fig.2 were further interpolated for better visualization.

OAM modal decomposition. OAM mode spectra are obtained by calculating the azimuthal Fourier transform of the measured spatiotemporal phase along the azimuthal direction in the x-t plane using normalized polar coordinates, $r_{norm} = \sqrt{(x/x_w)^2 + (ct/ct_w)^2}$ and $\phi_{norm} = \tan^{-1}[(x/x_w)/(ct/ct_w)]$. To calculate the normalization factors x_w and t_w for normalization, we first defined the origin of the polar coordinate as the position of the phase singularity (or the midpoint of multiple singularity positions), corresponding to the central minimum in the amplitude profile. Then a cross-section of the vortex, including the origin, was plotted along the x-axis and the t-axis. These cross-sections show two peaks, i.e., the front and rear ends of the wheel. We defined x_w and t_w to be one half of the peak-to-peak separation along the x- and t-axis, respectively. In Fig. 3c, the scaling factors were inherited from Fig. 3b, since the amplitude profile shown in Fig. 3c is not in an ideal vortex shape. The spectral resolution is limited to one, a quantized integer for the spatiotemporal topological charges. The plots are interpolated for smoothness.

Spatiotemporal momentum and energy density flows. The momentum and energy density flows are calculated based on the reconstructed phase in the x-t plane. The gradient operation is achieved by numerically calculating the differential of the phase, and applying a moving average to the resultant vector field to remove high frequency noise. The amplitude of the momentum density flow vectors $|\vec{P}|$, the length of the yellow arrows in Fig. 4a-4c, are scaled by $1/x_0,\ x_0 = 1.25\ mm$, on the x-axes and $1/ct_0, t_0 = 300\ fs$, on the ζ-axes for better visualization. On the contrary, the amplitude of the energy density flow vectors $|\vec{J}|$, the length of the cyan arrows in Fig. 4d-4f, are not scaled to show the original orientation of energy flow directly. The dominant but trivial linear momentum and energy density flow in the t (or z) direction is removed, respectively. The quantized charge ℓ is calculated by the 2D "volume" integration of the momentum density flows following the equation[12]: $\ell \equiv \hbar[\int \vec{r} \times \vec{P}\, dV] / [\int E^* E dV$.

Data Availability

The datasets utilized to prepare the data presented in this manuscript are available and free of charge from the corresponding author under reasonable request.

Reference

1. Coullet, P., GIL, L. & Rocca, F. Optical Vortices. *Opt. Commun.* **73**, 403–408 (1989).
2. Allen, L., Beijersbergen, M. W., Spreeuw, R. J. C. & Woerdman, J. P. Orbital angular momentum of light and the transformation of Laguerre-Gaussian laser modes. *Phys. Rev. A* **45**, 31–35 (1992).
3. Curtis, J. E. & Grier, D. G. Structure of Optical Vortices. *Phys. Rev. Lett.* **90**, 4 (2003).
4. Vaziri, A., Pan, J. W., Jennewein, T., Weihs, G. & Zeilinger, A. Concentration of higher dimensional entanglement: Qutrits of photon orbital angular momentum. *Phys. Rev. Lett.* **91**, 1–4 (2003).
5. B. Wang, M. Tanksalvala, Z. Zhang, Y. Esashi, N. Jenkins, M. Murnane, H. Kapteyn, and C.-T. L. Coherent Fourier scatterometry using orbital angular momentum beams for defect detection. *Submitted* (2020).
6. Padgett, M. J. Orbital angular momentum 25 years on. *Opt. Express* **25**, 11265 (2017).
7. Shen, Y. *et al.* Optical vortices 30 years on: OAM manipulation from topological charge to multiple singularities. *Light Sci. Appl.* **8**, (2019).
8. Sukhorukov, A. P. & Yangirova, V. V. Spatio-temporal vortices: properties, generation and recording. *Nonlinear Opt. Appl.* **5949**, 594906 (2005).
9. Bliokh, K. Y. & Nori, F. Spatiotemporal vortex beams and angular momentum. *Phys. Rev. A* **86**, 1–8 (2012).
10. Jhajj, N. *et al.* Spatiotemporal optical vortices. *Phys. Rev. X* **6**, 1–13 (2016).
11. Hancock, S. W., Zahedpour, S., Goffin, A. & Milchberg, H. M. Free-space propagation of spatiotemporal optical vortices. *Optica* **6**, 1547 (2019).
12. Chong, A., Wan, C., Chen, J. & Zhan, Q. Generation of spatiotemporal optical vortices with controllable transverse orbital angular momentum. *Nat. Photonics* **14**, 350–354 (2020).
13. Dholakia, K.; Simpson, N. B.; Padgett, M. J.; and Allen, L. Second-harmonic generation and the orbital angular momentum of light. *Phys. Rev. A* **54**, 3742–3745 (1996).
14. Courtial, J., Dholakia, K., Allen, L. & Padgett, M. J. Second-harmonic generation and the conservation of orbital angular momentum with high-order Laguerre-Gaussian modes. *Phys. Rev. A* **56**, 273–276 (1997).
15. Hernández-García, C., Picón, A., San Román, J. & Plaja, L. Attosecond extreme

ultraviolet vortices from high-order harmonic generation. *Phys. Rev. Lett.* **111**, 1–5 (2013).

16. Strohaber, J. *et al.* Coherent transfer of optical orbital angular momentum in multi-order Raman sideband generation. *Opt. Lett.* **37**, 3411 (2012).
17. Dorney, K. M. *et al.* Controlling the polarization and vortex charge of attosecond high-harmonic beams via simultaneous spin–orbit momentum conservation. *Nat. Photonics* **13**, 123–130 (2019).
18. Rego, L. *et al.* Generation of extreme-ultraviolet beams with time-varying orbital angular momentum. *Science.* **364**, (2019).
19. Bazhenov, V. Y., Soskin, M. S. & Vasnetsov, M. V. Screw dislocations in light wavefronts. *J. Mod. Opt.* **39**, 985–990 (1992).
20. Esashi, Y. *et al.* Ptychographic amplitude and phase reconstruction of bichromatic vortex beams. *Opt. Express* **26**, 34007 (2018).
21. Hickmann, J. M., Fonseca, E. J. S., Soares, W. C. & Chávez-Cerda, S. Unveiling a truncated optical lattice associated with a triangular aperture using light's orbital angular momentum. *Phys. Rev. Lett.* **105**, 1–4 (2010).
22. Hancock, S. W., Zahedpour, S. & Milchberg, H. M. Orbital angular momentum conservation in second- harmonic generation with spatiotemporal optical vortices. *Front. Opt. + Laser Sci. APS/DLS, OSA Tech. Dig. (Optical Soc. Am. 2020), Pap. FM7C.6.*
23. Speirits, F. C. & Barnett, S. M. Do waves carrying orbital angular momentum possess azimuthal linear momentum? *Phys. Rev. Lett.* **111**, 4–6 (2013).
24. Sidick, E., Knoesen, A. & Dienes, A. Ultrashort-pulse second-harmonic generation. I . Transform-limited fundamental pulses. *J. Opt. Soc. Am. B* **12**, 1704–1712 (1995).
25. Sidick, E., Dienes, A. & Knoesen, A. Ultrashort-pulse second-harmonic generation. II. Non-transform-limited fundamental pulses Erkin. *J. Opt. Soc. Am. B* **12**, 1713–1722 (1995).
26. Picón, A. *et al.* Photoionization with orbital angular momentum beams. *Opt. Express* **18**, 3660 (2010).
27. He, H., Friese, M. E. J., Heckenberg, N. R. & Rubinsztein-Dunlop, H. Direct observation of transfer of angular momentum to absorptive particles from a laser beam with a phase singularity. *Phys. Rev. Lett.* **75**, 199–202 (1995).

28. Paterson, L. *et al.* Controlled rotation of optically trapped microscopic particles. *Science.* **292**, 912–914 (2001).
29. MacDonald, M. P. *et al.* Creation and manipulation of three-dimensional optically trapped structures. *Science.* **296**, 1101–1103 (2002).
30. Vieira, J. & Mendonça, J. T. Nonlinear laser driven donut wakefields for positron and electron acceleration. *Phys. Rev. Lett.* **112**, 1–5 (2014).
31. Karimi, E., Marrucci, L., de Lisio, C. & Santamato, E. Time-division multiplexing of the orbital angular momentum of light. *Opt. Lett.* **37**, 127 (2012).
32. Vieira, J. *et al.* Amplification and generation of ultra-intense twisted laser pulses via stimulated Raman scattering. *Nat. Commun.* **7**, 1–7 (2016).
33. Tang, Y. *et al.* Harmonic spin–orbit angular momentum cascade in nonlinear optical crystals. *Nat. Photonics* **14**, 658–662 (2020).
34. Verbeeck, J., Tian, H. & Schattschneider, P. Production and application of electron vortex beams. *Nature* **467**, 301–304 (2010).
35. Chen, J., Wan, C., Chong, A. & Zhan, Q. Subwavelength focusing of a spatio-temporal wave packet with transverse orbital angular momentum. *Opt. Express* **28**, 18472 (2020).

Acknowledgments

The JILA authors gratefully acknowledge funding from an AFOSR MURI (FA9550-16-1-0121).

Author contributions

C.-T.L. conceived the project, G.G. conducted and designed the experiment, and both analyzed the data. M. M. M. and H. C. K. proposed the research thrust, supervised the research, developed the generation and measurement capabilities, and applications. All authors contributed to the discussion and writing of the manuscript.

Competing interests

M. M. M. and H. C. K. have a financial interest in KMLabs. The other authors declare no competing financial interests.

Corresponding Authors

Please address all correspondence to Chen-Ting Liao.

Figures

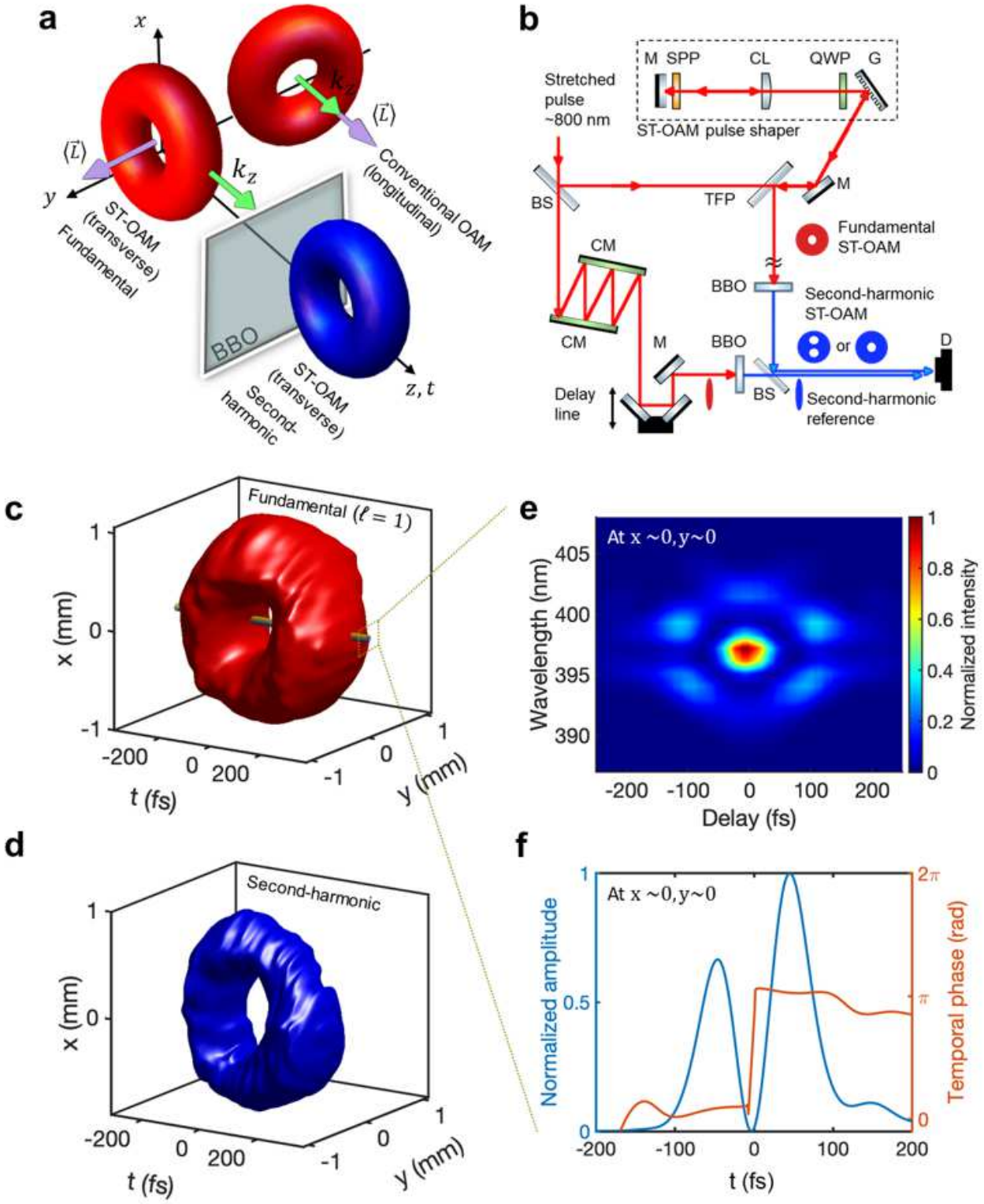

Figure 1

Second-harmonic spatiotemporal orbital angular momentum (ST-OAM) pulse generation and characterization. a. Schematic of longitudinal (conventional) OAM of light, transverse ST-OAM of light, and its second-harmonic generation (SHG). All pulses are represented by their isosurface intensity

profiles. The averaged OAM ⃗L ⃗ ⃗ (purple arrows) in a conventional OAM pulse is parallel to or aligned with the propagation direction (k_z) ⃗ (green arrows), and thus named longitudinal OAM, while the averaged OAM in an ST-OAM pulse is perpendicular to the propagation direction and thus named transverse OAM. b. In the experiment, fundamental ST-OAM pulses of topological charge ℓ =1 are generated by a custom pulse shaper. The pulses carry an azimuthal spatiotemporal phase swirl structure in the x-z plane, parallel to the beam propagation direction along the z-axis. Second-harmonic ST-OAM pulses are generated in a BBO crystal and then characterized by interference with a reference Gaussian pulse. c. Experimentally reconstructed 3D intensity isosurface profile of the fundamental ST-OAM pulse and its second-harmonic shown in d. The intensity profile shows a singularity structure in space and time at the center. The center part of the fundamental ST-OAM pulse (indicated by the brown bar) was experimentally sampled and charactered by a FROG setup, where the measured FROG trace and the reconstructed temporal electric field envelope and the temporal phase are shown in e and f, respectively. M: mirror; DM: dichroic mirror; CM: chirped mirror; CL: cylindrical lens; BS: beam splitter; TFP: thin film polarizer; QWP: quarter wave plate; SPP: spiral phase plate; G: grating; BBO: beta barium borate crystal; D: detectors including a beam profiler and a FROG setup.

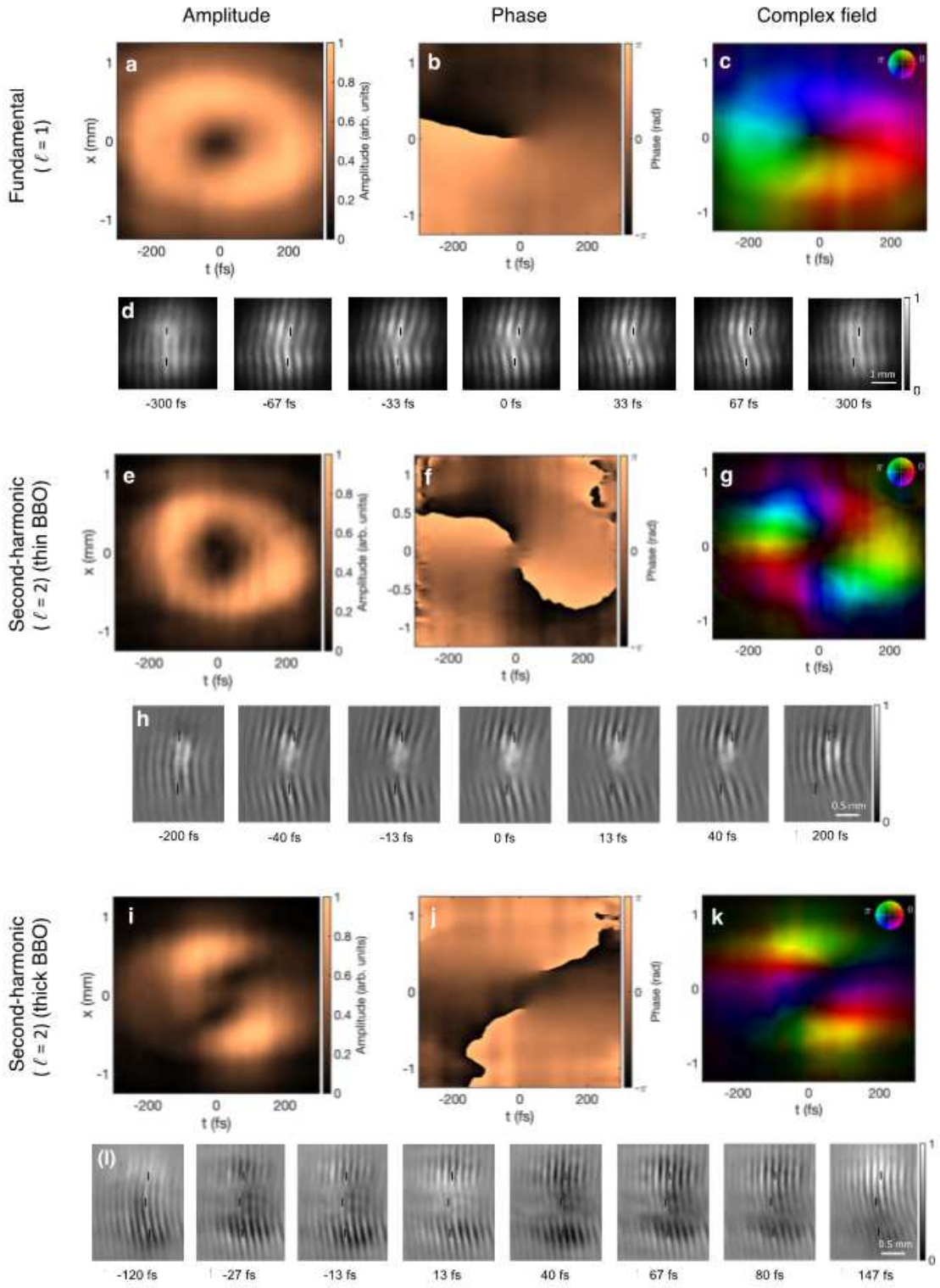

Figure 2

Experimentally reconstructed amplitude and phase of ST-OAM pulses. A fundamental ST-OAM pulse of topological charge ℓ =1 was measured and reconstructed to show its a, amplitude envelope, b, phase, and c, complex field representation by a scanning interferometer. Representative fringe patterns at various time delays obtained from the interferometry are shown in d, with two black markers added as an aid to the eye to observe the fringe shift. The phase profile in a fundamental ST-OAM pulse shows the 2π spiral

phase accumulation on traversing a closed spatiotemporal path around the singularity. A second-harmonic ST-OAM pulse generated by a thin BBO crystal was measured and reconstructed using the same method to show its d, amplitude envelope, e, phase, f, complex field representation, and g. representative fringe patterns. The results show that the spatiotemporal topological charge is also doubled after frequency doubling, evidenced by the 4π phase accumulation. The SHG with topological charge ℓ =2 indicates the conservation of ST-OAM. A second-harmonic ST-OAM pulse was also generated by a thick BBO crystal and measured in h, amplitude envelope, i, phase, j, complex field representation, and k, representative fringe patterns. The OAM is still conserved in this case, but the two singularities are generated and separated further in both space and time, comparing to the case in a thin BBO crystal. The color wheels for complex field representation are shown at the top right corners of a, g, k, where amplitude and phase are represented by brightness and hue, respectively.

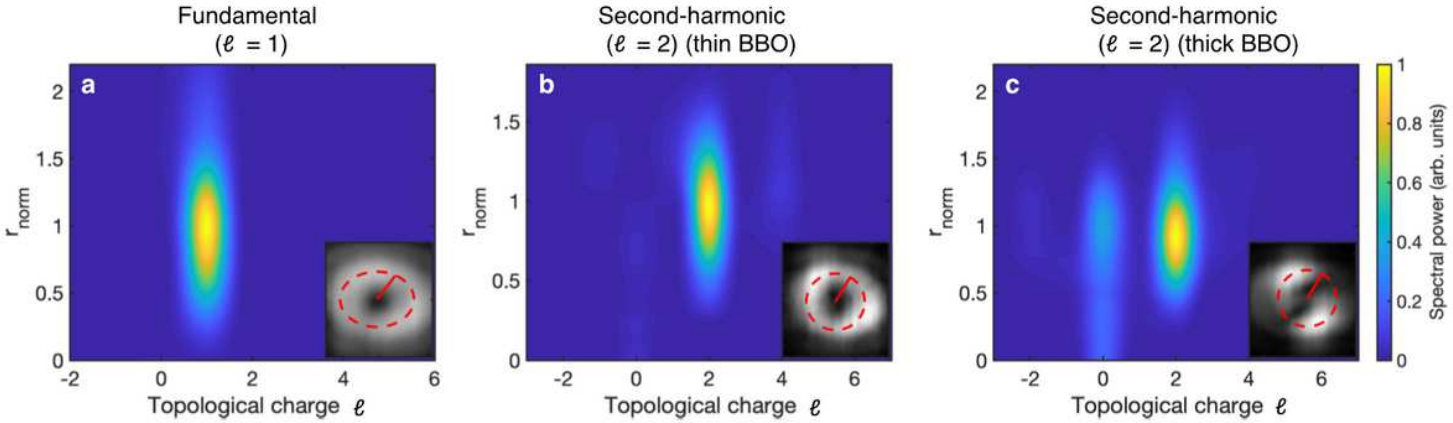

Figure 3

Modal decomposition of the ST-OAM pulses. OAM mode spectra of the ST-OAM pulses from a, fundamental pulses, b, second-harmonic pulses generated by a thin BBO, and c, second-harmonic pulses generated by a thick BBO. The modal decompositions are obtained by Fourier transformation of the measured spatiotemporal phase along the azimuthal direction on the x-t plane for different normalized polar radii r_norm. The radii are shown in solid red lines in the insets overlapped with their corresponding amplitude envelope profiles for reference. The color map corresponds to the power spectrum in arbitrary units. In a, the ℓ = 1 charge contains ~94.5% of the total spectral power. In b and c, the ℓ = 2 charge contains ~80.9% and ~57.8% of the total power, respectively.

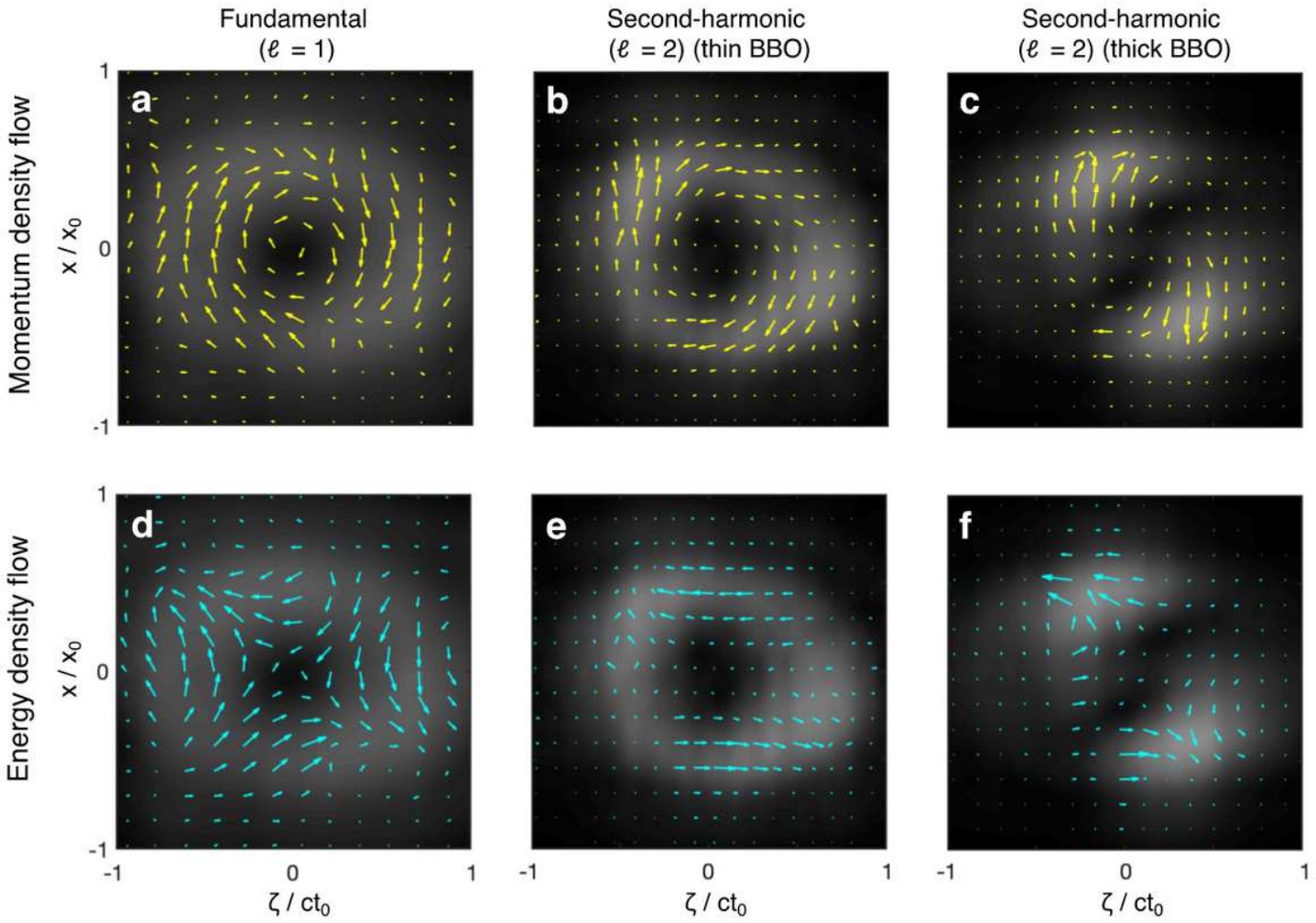

Figure 4

Spatiotemporal momentum and energy density flows of ST-OAM pulses. A momentum density flow, which is proportional to the imaginary part of the scalar field complex conjugate multiplying the field gradient, is calculated in a, a fundamental ST-OAM pulse, b, its second-harmonic ST-OAM pulse generated by a thin BBO crystal, and c, its second-harmonic ST-OAM pulse generated by a thick BBO crystal. The ratio of ST-OAM per pulse I^2ω/I^ω is 2.09, comparing b. to a., and 1.36,comparing c.to a. An energy density flow in the BBO crystal, which is proportional to the phase gradient and the dispersion, is calculated in d, a fundamental ST-OAM pulse, e, its second-harmonic ST-OAM pulse generated by a thin BBO crystal, and f, its second-harmonic ST-OAM pulse generated by a thick BBO crystal. The amplitude of the momentum density flow vectors (the length of the yellow arrows) are scaled by 1/ct_o along the ζ-axes and by 1/x_0 along the x-axis for better visualization. On the contrary, the amplitude of the energy density flow vectors (the length of the cyan arrows) is not scaled to show the original orientation of energy flow directly. The grayscale backgrounds are amplitude envelope profiles taken from Fig. 2a, 2e, 2i for reference. ST OAM pulses propagate from the left to the right of the figures.